COMPLEX TURBULENT COMPRESSIBLE FLOW COMPUTATION USING A TWO-LAYER APPROACH

BIJAN MOHAMMADI

INRIA-MENUSIN, Domaine de Voluceau, BP 105, F-78153 Le Chesnay, France

SUMMARY

A two-layer approach is proposed to compute complex flows including separations. For high- and low-Reynolds-number regions we use a two-equation k–ε model and a one-equation k–L model respectively. A robust algorithm is proposed for the treatment of the convective part of the turbulence equations. Several complex configurations including separations are computed.

KEY WORDS   Turbulence   Two-equation model   Two-layer approach

1. INTRODUCTION

The success of turbulence modelling and simulation depends greatly on the treatment of near-wall regions. The classical wall-law technique is based on the assumption that there exist universal laws related to a turbulence in equilibrium near the wall. This approach avoids the solution of the Navier–Stokes equations and turbulence models in the near-wall regions. However, such a technique fails when separation occurs. On the other hand, the modified low-Reynolds-number two-equation models which are valid up to the wall can be employed.[1] Patel *et al.* have concluded that even for simple configurations these models are not entirely satisfactory.[1] Furthermore, a computation using such a model requires considerably more grid points. This is because the turbulent quantities (especially ε) have very large gradients in the sublayer. Therefore the use of these models in more complex situations may introduce uncertainties and the solution may be mesh-dependent.

In this paper we propose to extend the two-layer approach[2] to compressible configurations. This technique is more complicated than a simple wall-law technique but more practical than a low-Reynolds-number two-equation model. In particular, the model is less mesh-dependent and numerically more stable. Hence a two-equation model is used for high-Reynolds-number regions and a one-equation model near the solid wall. For the two-equation model the compressible version of the k–ε turbulence model is used as in Reference 3. This model is directly obtained from the incompressible version of the model. The convective parts of the equations are treated by a method of characteristics and the source terms are treated during this step. In the one-equation model we have a transport equation for one turbulence scale and the other scale is computed by an algebraic expression.

In Section 2 we describe the Navier–Stokes equations and the turbulence models which we used. Section 3 is devoted to the description of the numerical methods. In Section 4 several test cases including separation are presented and it is shown that the two-layer approach combined with our algorithm for the k–ε equations resolves the major difficulties encountered in turbulent flow computation with two-equation models.

2. THE TURBULENT AND MEAN FLOW EQUATIONS

Let ρ be the density, u the velocity, T the temperature, $E = T + \|u\|^2/2$ the total energy, $p = (\gamma - 1)\rho T$ the pressure, $\nabla u = u_{i,j}$ the gradient of u, $D = u_{i,i}$ its divergence, $S = (\nabla u + \nabla u^{\mathrm{T}}) - \frac{2}{3}D$ the deformation tensor and $F = S : \nabla u$.

2.1. The averaged Navier–Stokes equations

We split all the variables into mean and fluctuating parts. We use the Reynolds average for the density and pressure and the Favre average for the other variables and we then consider the Reynolds-averaged Navier–Stokes equations. Once the unknown correlations are modelled as in Reference 3, we have

$$\frac{\partial \rho}{\partial t} + \nabla \cdot (\rho u) = 0,$$

$$\frac{\partial \rho u}{\partial t} + \nabla \cdot (\rho u \otimes u) + \nabla p_{\mathrm{t}} = \nabla \cdot [(\mu + \mu_{\mathrm{t}}) S],$$

$$\frac{\partial \rho E_{\mathrm{t}}}{\partial t} + \nabla \cdot [(\rho E_{\mathrm{t}} + p_{\mathrm{t}}) u] = \nabla \cdot [(\mu + \mu_{\mathrm{t}}) S u] + \nabla [(\kappa + \kappa_{\mathrm{t}}) \nabla T],$$

with

$$p_{\mathrm{t}} = p + \tfrac{2}{3}\rho k, \qquad E_{\mathrm{t}} = E + k,$$

$$\kappa = \frac{\gamma \mu}{Pr}, \qquad \kappa_{\mathrm{t}} = \frac{\gamma \mu_{\mathrm{t}}}{Pr_{\mathrm{t}}},$$

$$\gamma = 1\cdot 4, \qquad Pr = 0\cdot 72, \qquad Pr_{\mathrm{t}} = 0\cdot 9,$$

where μ_{t} and k are the eddy viscosity and the turbulent kinetic energy respectively. As in Reference 3, we suppose that the turbulent contributions to the pressure and the total energy are negligible, so,

$$E_{\mathrm{t}} = E, \qquad p_{\mathrm{t}} = p.$$

Indeed, these turbulent contributions do not play an essential role except in highly sheared regions. Hence the coupling between the turbulent and mean flow equations is taken into account only through the viscosity. Moreover, this enables us to have the same constitutive law as in the laminar case. Another reason is that in our k–ε model several compressibility effects are not taken into account. Therefore k will probably be unpredicted in regions where compressibility effects are important. Thus the introduction of a wrong turbulent kinetic energy in the mean computation may produce uncertainties.

2.2. Turbulence models

It is well known that turbulence modelling when the Reynolds number is high is easier than when it decreases. For example, the high-Reynolds-number hypothesis allows us to ignore several unknown correlations in the non-modelled k-equation. In the same way the presumed analogy between the k- and ε-equations is only valid in the high-Reynolds-number case. However, when the Reynolds number decreases, the behaviour of the different unknown correlations is not clear.

2.3. The high-Reynolds-number k–ε model

Because of the hypothesis of equilibrium between production and destruction of turbulence, the classical k–ε model is only valid in fully turbulent regions. Therefore we will use it only when we are sure that viscous effects are not dominant (e.g. for $y^+ \geqslant 200$). The k–ε equations we consider are

$$\frac{\partial k}{\partial t} + u\nabla k - \frac{1}{\rho}\nabla\left(c_\mu\rho\frac{k^2}{\varepsilon}\nabla k\right) = S_k, \tag{1}$$

$$\frac{\partial \varepsilon}{\partial t} + u\nabla\varepsilon - \frac{1}{\rho}\nabla\left(c_\varepsilon\rho\frac{k^2}{\varepsilon}\nabla\varepsilon\right) = S_\varepsilon. \tag{2}$$

The right-hand sides of (1) and (2) contain the production and destruction terms for k and ε,

$$S_k = c_\mu\frac{k^2}{\varepsilon}F - \tfrac{2}{3}kD - \varepsilon, \tag{3}$$

$$S_\varepsilon = c_1 kF - \frac{2c_1}{3c_\mu}\varepsilon D - c_2\frac{\varepsilon^2}{k}, \tag{4}$$

where c_μ, c_1, c_2 and c_ε are 0·09, 0·129, 1·92 and 0·07 respectively. The eddy viscosity is given by

$$\mu_t = c_\mu\rho\frac{k^2}{\varepsilon}.$$

As in Reference 3, in our version of the k–ε model we have completely neglected the trace of the pressure–strain tensor and the scalar product of pressure gradient and Favre-averaged velocity fluctuation,

$$\overline{p'\nabla\cdot u''} - \overline{u''}\nabla\bar{p},$$

where $\bar{a}$ denotes the Reynolds average of a $(a = \bar{a} + a')$ and a'' is the Favre-averaged fluctuation.

2.4. Low-Reynolds-number case

The previous k–ε model is established under the hypothesis that the local Reynolds number is high. However, near a solid wall the local Reynolds number decreases, so to compute flow adjacent to a wall, we have to use a different approach. The most classical technique is to replace the boundary of the computational domain a small distance away from the wall and to simulate the action of the wall on the flow using slip boundary conditions. Using this technique in Reference 3, we managed to compute attached flows, but to compute complex flows where separation occurs, this technique fails. On the other hand, because of the complexity of the situations we consider, a modified low-Reynolds-number k–ε model will require too fine a mesh. Moreover, we are not really interested in the exact description of the flow field or the turbulent quantities in the sublayer. Thus we prefer an intermediate solution which consists of computing the flow up to the wall using a two-layer approach. Hence for near-wall regions (e.g. $y^+ \leqslant 200$) a one-equation k–L model and for regions away from the wall the classical k–ε model described above are applied. The one-equation k–L turbulence model consists of one transport equation for the turbulent kinetic energy k,

$$\frac{\partial k}{\partial t} + u\nabla k - \frac{1}{\rho}\nabla\cdot(\mu_t\nabla k) = \mu_t F - \tfrac{2}{3}Dk - \text{Diss}, \tag{5}$$

where

$$\text{Diss} = \frac{k^{3/2}}{l_\varepsilon} \qquad (6)$$

is the dissipation of the turbulent kinetic energy, $\mu_t = c_\mu \rho k^{1/2} l_\mu$ is the eddy viscosity and l_μ and l_ε are two length scales which contain the damping effects in the near-wall regions:

$$l_\mu = \kappa c_\mu^{-3/4} y \left[1 - \exp\left(-\frac{y^+}{70} \right) \right], \qquad (7)$$

$$l_\varepsilon = \kappa c_\mu^{-3/4} y \left[1 - \exp\left(-\frac{y^+}{2\kappa c_\mu^{-3/4}} \right) \right]. \qquad (8)$$

In the previous expression the local Reynolds number $y^+ = k^{1/2} \rho y / \mu$ depends on the local turbulence intensity ('w' means at the wall) and on the distance y from the wall. This avoids the use of friction at the wall (u_τ), which is computed using the mean flow field.

3. STABILITY IMPROVEMENT

Implementing the k–ε model in a finite element framework involves several difficulties. The most important among these is, from the numerical point of view, the high instability of the discretized k–ε equations. In References 4 and 5 the authors describe several difficulties encountered in the implementation of the k–ε model in their solvers. To avoid such a problem, a classical technique consists of introducing artificial diffusivity in the streamline directions or modifying the diffusion constants in the k- and ε-equations to stabilize the discretized system. Our experience shows that the k–ε system must be solved by a 'physical' method. Indeed, classical methods for solving non-linear problems (explicit or Newton steps) fail to converge or generate negative values of k and ε. We believe that the method must stay in close connection with the flow description. For this reason we prefer a characteristic Galerkin method. Hence we follow the evolution of the turbulent quantities along the streamlines. Moreover, we know that the difficulties come from the resolution of the dynamical part (i.e. the convective operator and the source terms) of the equations and the viscous part is not really difficult to solve (by classical centered schemes). Therefore we study this dynamical part more carefully. In other words, let

$$\frac{\partial k}{\partial t} + u\nabla k = c_\mu \frac{k^2}{\varepsilon} F - \tfrac{2}{3} kD - \varepsilon \qquad (9)$$

and

$$\frac{\partial \varepsilon}{\partial t} + u\nabla \varepsilon = c_1 kF - \frac{2c_1}{3c_\mu} \varepsilon D - c_2 \frac{\varepsilon^2}{k} \qquad (10)$$

be the dynamical parts of the k- and ε-equations. Several authors have proposed combinations of k and ε which are more interesting for numerical applications. In References 3 and 6 we proposed a new pair of variables and showed that the corresponding system is more stable. We denote $d/dt = \partial/\partial t + u\nabla$. Let

$$\theta = \frac{k}{\varepsilon}, \qquad \varphi = \frac{\varepsilon^2}{k^3}. \qquad (11)$$

The dynamical θ- and φ-equations become from (9) and (10)

$$\frac{d}{dt}\theta = -aF\theta^2 + bD\theta + c, \qquad (12)$$

and

$$\frac{\mathrm{d}}{\mathrm{d}t}\varphi = -\alpha F\varphi\theta + \beta D\varphi - \delta\frac{\varphi}{\theta},\tag{13}$$

where $a = c_1 - c_\mu$, $b = \frac{2}{3}(c_1/c_\mu - 1)$, $c = c_2 - 1$, $\alpha = 3c_\mu - 2c_1$, $\beta = 2 - 2c_1/3c_\mu$ and $\delta = 2c_2 - 3$ are positive constants. F is always positive. Indeed,

$$F = (\nabla u + \nabla u^{\mathrm{T}} - \tfrac{2}{3}DI):\nabla u.$$

Thus, if $u = (v, w)$, then

$$F = \tfrac{2}{3}(v_{,x} - w_{,y})^2 + (w_{,x} + v_{,y})^2 \geqslant 0.$$

Therefore θ stays bounded and positive.[3] The φ-equation (13) can also be integrated along the characteristic curves. Its solution for a positive initial condition $\varphi_0 = \varepsilon_0^2/k_0^3$, is

$$\varphi = \varphi_0 \exp\left[\left(-\alpha F\theta + \beta D - \frac{\delta}{\theta}\right)t\right].$$

Therefore φ stays positive and bounded if D is such that

$$D \leqslant \frac{\alpha F\theta}{\beta} + \frac{\delta}{\beta\theta}.$$

Thus for compression cases φ always stays bounded and positive, but for strong expansion situations φ may behave exponentially. This is somewhat natural because several compressibility effects are not taken into account by the model.[3]

In the low-Reynolds-number case ($y^+ \leqslant 200$) we can also find equations for θ and φ. Indeed, by (6) we have

$$\varphi = \frac{1}{l_\varepsilon^2}, \qquad \theta = \frac{l_\varepsilon}{k^{1/2}}.$$

Thus, using (5)–(8), we obtain

$$\frac{\mathrm{d}}{\mathrm{d}t}\varphi = -A_1 \frac{\mathrm{d}}{\mathrm{d}t}k,\tag{14}$$

$$\frac{\mathrm{d}}{\mathrm{d}t}\theta = A_2 \frac{\mathrm{d}}{\mathrm{d}t}k,\tag{15}$$

with A_1 and A_2 given by

$$A_1 = \frac{\rho_w}{2\mu_w y^2 l_\varepsilon^3 k^{1/2}} \exp\left(-\frac{y^+}{2C_1}\right)$$

$$A_2 = \left[\frac{\rho_w y^2}{2\mu_w k} \exp\left(-\frac{y^+}{2C_L}\right) - \frac{l_\varepsilon}{2C_1}\right].$$

A_1 is always positive but the sign of A_2 is not known a priori. Thus the behaviour of φ and θ changes in the low-Reynolds-number regions. This is in agreement with the fact that the k–ε model is not valid in the near-wall region. Indeed, the nature of the equations changes from one region to the other. Thus we use the previous stability analysis only for the fully turbulent regions. We will now describe the numerical techniques which we used to solve the turbulent equations.

4. RESOLUTION SCHEME

The numerical techniques are the same as those developed in Reference 3. We perform a splitting between the Navier–Stokes and turbulent equations and search for a steady solution by an iterative scheme. In other words, at each iteration the turbulent solver gives a new viscosity to the Navier–Stokes solver until convergence. The Navier–Stokes equations are solved by an implicit upwind solver using an Osher–Riemann solver for the convective part of the equations[7] or a Lax–Wendroff scheme.[8,9] Moreover, we use a local time step technique. This time step may be reduced by the k–ε solver for reasons of stability.

4.1. The turbulent solver

To solve the k–ε equations, we perform a splitting between the transport and diffusion parts of the equations. The transport part of the equations is solved by a characteristic Galerkin method and we treat the source terms during this step. For points which are in the high-Reynolds-number regions the equations for the new variables φ and θ are used in place of those for k and ε. The diffusion part of the equations is solved by a classical P^1 finite element technique.

Notations. We denote by S_k^+ and S_k^- (resp. S_ε^+ and S_ε^-) the positive and negative parts of $S_k = S_k^+ - S_k^-$ (resp. S_ε); $k^n(X^n(\tau))$ (resp. $\varepsilon^n(X^n(\tau))$) is the value of k^n (resp. ε^n) at the beginning of the characteristic curve.

1. Time step reduction
Consider the following transport equation $(\mathrm{d}/\mathrm{d}t = \partial t + \partial u \nabla \cdot)$:

$$\frac{\mathrm{d}a}{\mathrm{d}t} = f = f^+ - f^-. \tag{16}$$

We require positivity of $a^{n+1/2}$ if a^n is positive and we write $f^n = f^{+n} - f^{-n}$ as

$$f^{+n}\frac{a^{n+1/2}}{a^n} - f^{-n}\frac{a^{n+1/2}}{a^n}.$$

Using the characteristic method, a possible scheme to solve (16) is then (to first order)

$$a^{n+1/2} = \frac{a^n(X^n)}{1 + (\Delta t/a^n)(f^{-n} - f^{+n})}. \tag{17}$$

Thus if a^n is positive, the positivity of $a^{n+1/2}$ is guaranteed always if $f^{-n} \geqslant f^{+n}$. However, if $f^{+n} > f^{-n}$, the positivity is obtained under the following limitation for the time step:

$$\Delta t \leqslant \frac{a^n}{f^{+n} - f^{-n}}. \tag{18}$$

2. How to compute y^+
To compute y^+, we need for each point in the mesh its normal distance to the wall, y. Thus we compute the minimum distance between the points and the wall nodes and we use this quantity instead of y. Our experience is that despite this not being exact, it is sufficient and the method is not greatly affected by this operation. Another remark is on the convenience of the method: we do not need the friction at the wall to compute y^+.

Knowing ρ^n, u^n, k^n and ε^n, we propose the following algorithm to compute the turbulent quantities at step $n+1$.

Algorithm (k, ε)

1. Compute $k^n(X^n)$ and $\varepsilon^n(X^n)$ (i.e. convect k^n and ε^n).
2. If $y^+ > 200$ (i.e. points where the local Reynolds number is high), then
   (a) if necessary, reduce the time step locally by (18) applied to (12) and (13)
   (b) compute $\theta^{n+1/2}$ and $\varphi^{n+1/2}$ by (17)
   (c) compute $k^{n+1/2}$ and $\varepsilon^{n+1/2}$ by

$$k^{n+1/2} = (\theta^{n+1/2})^{-2}(\varphi^{n+1/2})^{-1}, \qquad \varepsilon^{n+1/2} = (\theta^{n+1/2})^{-3}(\varphi^{n+1/2})^{-1}.$$

3. If $y^+ \leqslant 200$, then consider the dynamical part of the low-Reynolds-number k-equation (7). If needed, reduce the time step by (18) and compute directly $k^{n+1/2}$ by (17) and $\varepsilon^{n+1/2}$ by (8).
4. Solve

$$\frac{k^{n+1}}{\Delta t} - \frac{1}{\rho^n} \nabla \cdot [(\mu + \mu_t^n)\nabla k^{n+1}] = \frac{k^{n+1/2}}{\Delta t}, \tag{19}$$

$$\frac{\varepsilon^{n+1}}{\Delta t} - \frac{1}{\rho^n} \nabla \cdot [(\mu + c_\varepsilon \mu_t^n)\nabla \varepsilon^{n+1}] = \frac{\varepsilon^{n+1/2}}{\Delta t}. \tag{20}$$

Equations (19) and (20) are solved by a classical finite element method on P^1-triangles. Moreover, mass lumping should be used. This treatment of the diffusion guarantees the positivity and boundedness of the solution, for Dirichlet boundary conditions, only if there is no obtuse angle in the meshes for all values of Δt, F and D. It is the characteristic method that leads us to the stability analysis used here. For this reason it is hard to adapt this algorithm to other methods.

5. NUMERICAL RESULTS

In this section we consider three test cases including separation and recirculation. The first test case consists of the flow over a cylinder. It is well known that this case is unsteady, so we will see that using a steady approach, the flow which we compute corresponds more to a situation with a splitter plate in the wake. The other cases are flow over compression ramps in supersonic and hypersonic ranges. We show that the two-layer approach is quite promising for treating such complex flows.

5.1. Flow over a cylinder

We present numerical calculations of the flow past a circular cylinder in the subcritical Reynolds number range. The Reynolds number is $5 \times 10^4 \, \text{m}^{-1}$ and we consider a subsonic situation ($M_\infty = 0.5$). The diameter of the cylinder is 2 m.

Our aim is to observe the dependence of the results upon the mesh and, if possible, to obtain mesh-independent results. The time-averaged Navier–Stokes equations are solved using a finite volume solver based on a Lax–Wendroff scheme. Because of the time-averaged equations under consideration and because our solver is only first-order-accurate in time, we are interested in a steady state. However, it is well known that the flow behind a cylinder is unsteady. We consider then the flow past only half a circular cylinder. Our purpose is not to obtain good agreement with the data. Indeed, it seems that[10] the computation of the flow past a cylinder requires an unsteady solver because the vortex-shedding phenomenon has a very great impact on the results. Rather, we want to study the robustness of the k–ε solver on quite a hard test case and the quasi-independence of the results upon the mesh using a two-layer approach.

We present two computations for the same data on different meshes. For both computations we use polar grids extending to 10 diameters away from the cylinder and having respectively 70×70 and 80×110 nodes. Following Majumdar and Rodi,[10] because in the subcritical Reynolds number range the attached boundary layer is laminar, we introduce a switch to force the eddy viscosity to zero in the first quarter of the computational domain. Indeed, the k–ε model produces a very high level of turbulence in front of the cylinder and in this zone the variation in the velocity is large because the flow arrives at the body. However, the flow is clearly laminar.

On the cylinder, u and k are set to zero. For the velocity a symmetry boundary condition ($\mathbf{u} \cdot \mathbf{n} = 0$) and for the turbulent quantities a homogeneous Neumann boundary condition are applied on the centre-line. Dirichlet boundary conditions are used for all the variables on the first quarter of the external boundary ($0° \leqslant \omega \leqslant 90°$), i.e.

$$u = 1, \qquad v = 0, \qquad k = k_{\text{in}}, \qquad \varepsilon = \varepsilon_{\text{in}},$$

and a homogeneous Neumann boundary condition is used for the rest of the external boundary.
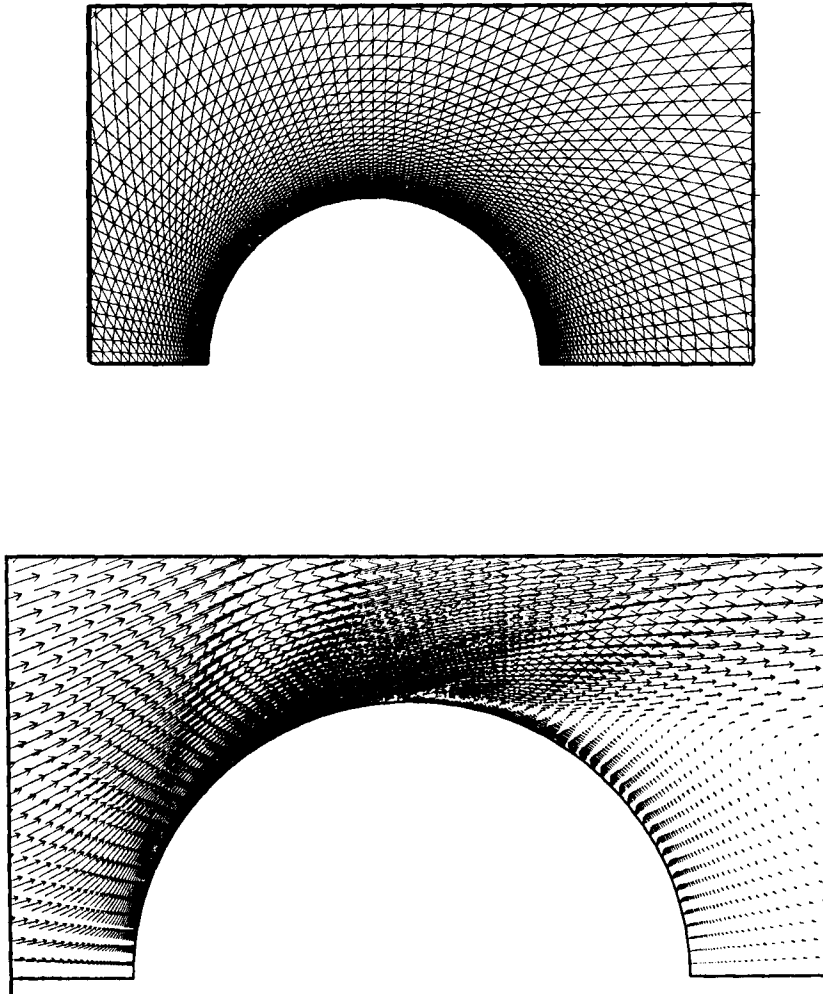
Figure 1. Partial view of the 70×70 polar grid and the velocity distribution around the cylinder

We begin the computation with a uniform flow. In particular, k and ε are initialized by k_{in} and ε_{in}. Two computations are done with $10^{-4}u_\infty^2$ and $10^{-3}u_\infty^2$ as initial and inlet values for k and ε. It seems that the levels of k_{in} and ε_{in} do not have a great impact on the results. The results we present are computed with $k_{in} = \varepsilon_{in} = 10^{-3}u_\infty^2$.

A plot of a partial view of the 70×70 grid and the velocity distribution around the cylinder are given in Figure 1. The calculated wall pressure coefficient C_p and wall friction coefficient C_f are given in Figure 2. These results are compared with available experimental data.[11] We can see that the base pressure is overestimated, especially in the separation region, and the skin friction is deceptive too. However, these results show that the solution is quite mesh-independent.
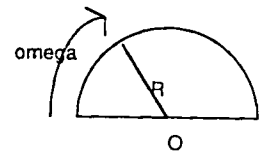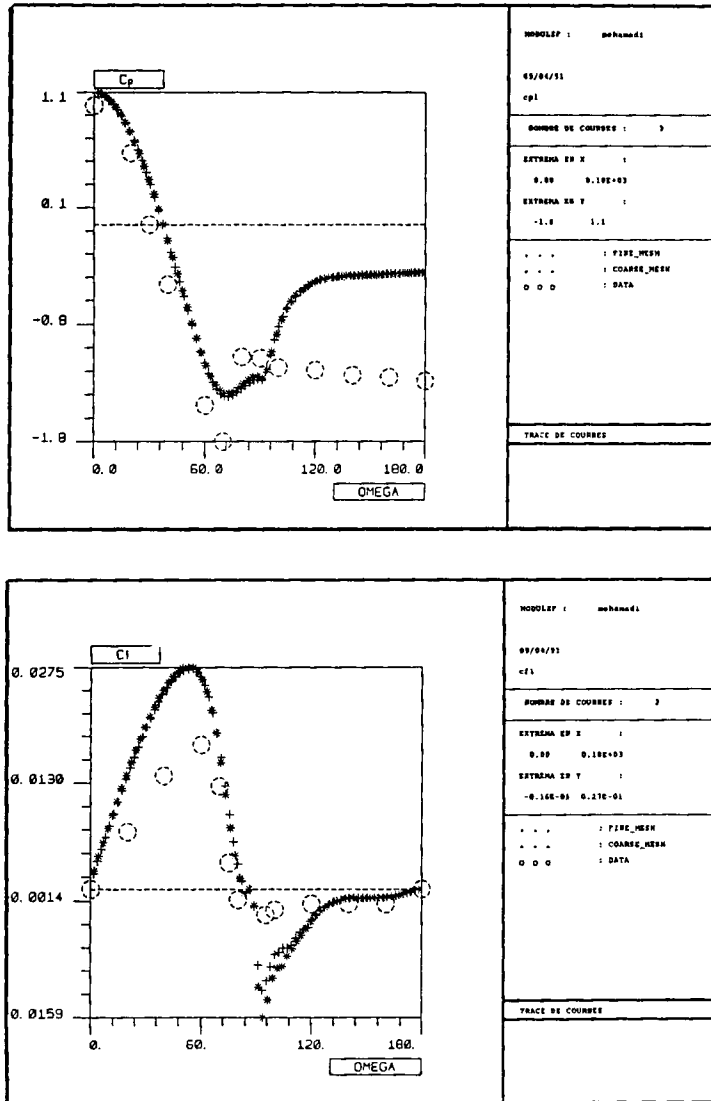
Figure 2. Distributions of C_p (top) and C_f (bottom) on the cylinder: $+$, fine; $*$, coarse; $\bigcirc$, data

Contour plots of the Mach number and C_p computed on the fine mesh are given in Figure 3. Contours of the turbulent kinetic energy k and the ratio of eddy viscosity to laminar viscosity (μ_t/μ) are shown in Figure 4. The eddy viscosity has a level between zero and $700\mu_1$. This is less than the level presented by Majumdar and Rodi[10] (between zero and $1600\mu_1$).

As pointed out by Majumdar and Rodi,[10] the computation of the flow past a circular cylinder is not possible without a time-dependent solver. The fine computation has taken about 2 h on a CRAY-2. The Navier–Stokes mean flow solver is vectorized while the turbulent solver works in scalar mode (in principle the characteristic method is not vectorizable because there are a lot of
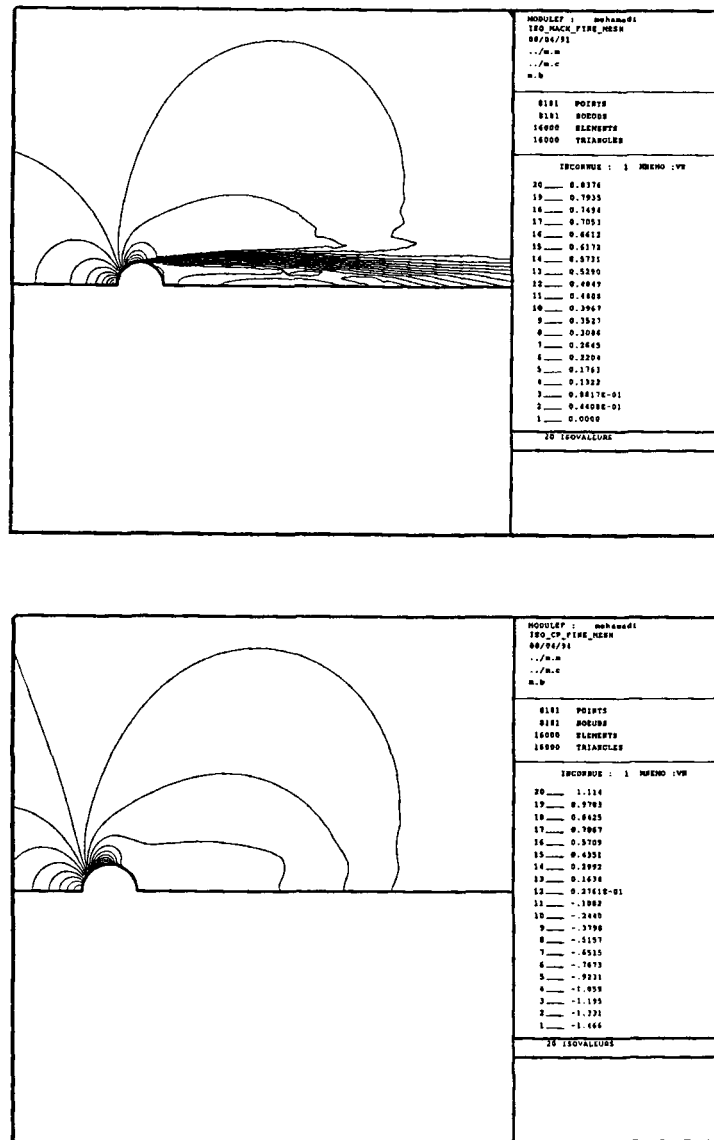
Figure 3. Contour plots of Mach number (top) and C_p (bottom)
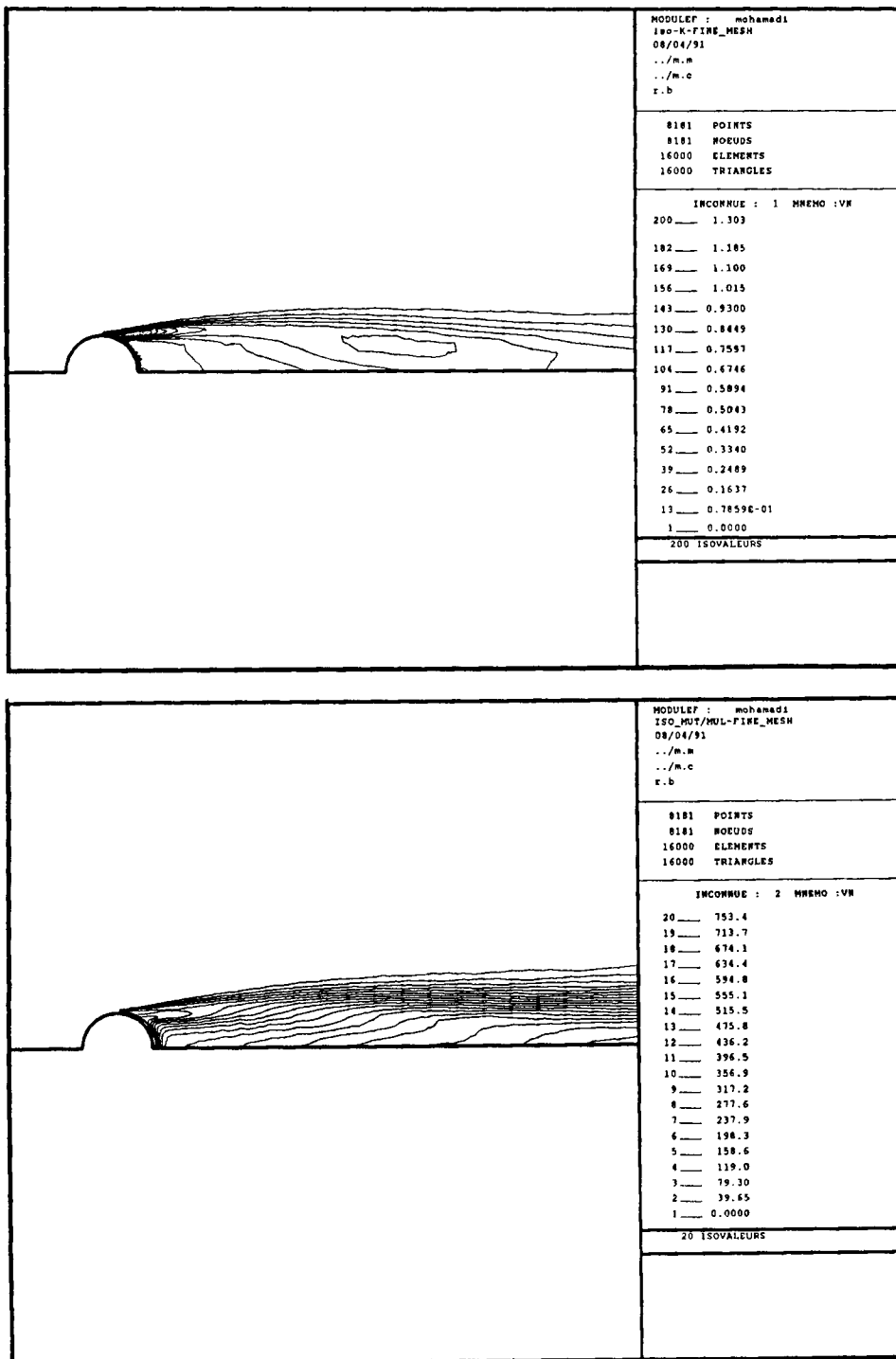
Figure 4. Contour plots k (top) and μ_t/μ_l (bottom)

geometrical tests). Thus the turbulent computation takes about one-third of the total CPU time. At this moment we have concentrated our efforts on the quality of the results rather on the reduction of the computational cost.

This computation shows that the two-layer approach combined with our algorithm enables us to compute such a complex flow without supplementary attention. Indeed, before using the mixed algorithm, we had never managed to compute such a flow without using limiters on k and ε. On the other hand, in this computation no positivity or boundedness problems have been encountered.

Finally, it is surprising to see that the flow stays subsonic. Indeed, the corresponding Euler computations show that at $M_\infty = 0.5$ the flow is transonic.[12]

5.2. Supersonic compression corner

This test case consists of a 35° supersonic compression corner (test case 3.3 of the Workshop on Hypersonic Flows for Reentry Problems, Antibes, January 1990). The Mach number is 5 and the
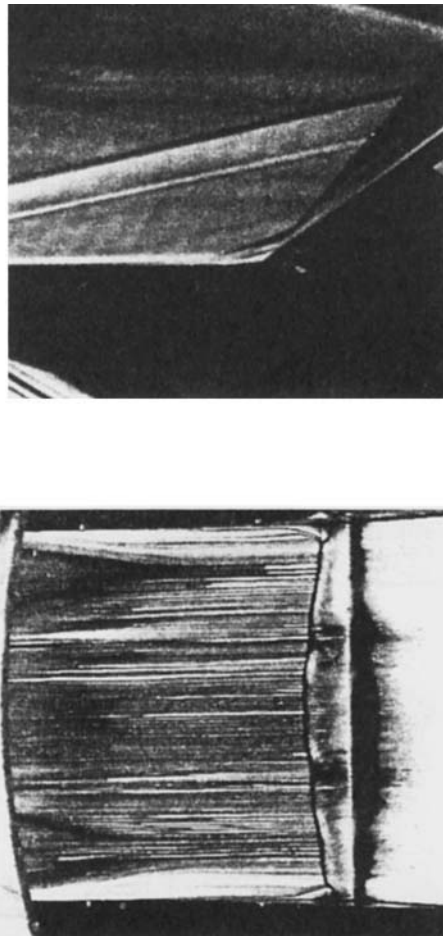
Figure 5. Surface flow visualizations ($M_\infty = 5$, $Re_\infty = 4 \times 10^7$ m^{-1})

Reynolds Number 4×10^7 m^{-1}. The free stream temperature is $T_\infty = 83 \cdot 6$ K and the wall temperature $T_w = 288$ K. Experiments have been carried out by Deléry and Coet at ONERA.[13] The overall flow organization is shown by a Schlieren photograph (Figure 5).

We have used two turbulence models: a Cebeci–Smith turbulence model including Goldberg's modification (see Appendix) and our k–ε model. For the k–ε computation we assume that the flow is laminar before $x_t = 0 \cdot 08$ ($Re_{x_t} = 3 \cdot 2 \times 10^5$). We take into account the transitional effect by varying the eddy viscosity from zero to μ_t between x_t and $2x_t$. Figure 6 gives a partial view of the refined mesh. It has 5067 nodes and 9792 triangles. This grid is obtained from a Cartesian one by a refinement process.[14, 15] The corner is at $x = 0 \cdot 25$ m from the leading edge. The first mesh spacing from the wall is 10^{-5} m. The computations are initialized by a uniform state based on the inlet values. The effects of the initial and inlet levels of the turbulent quantities are studied. Free
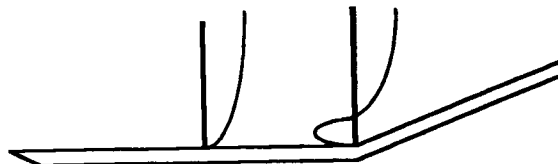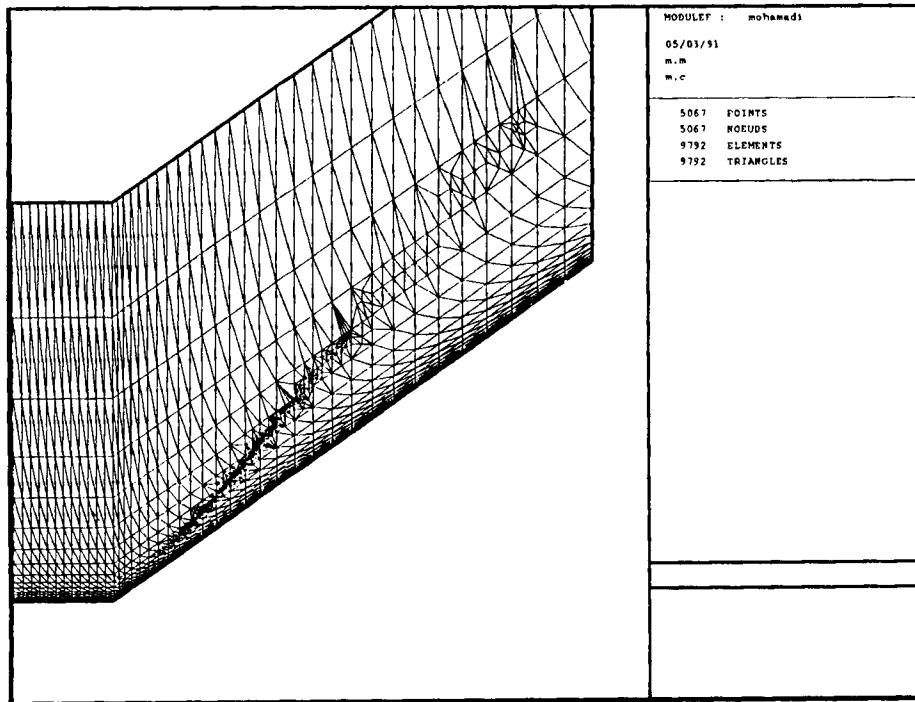
x=0.15   x=0.25

Figure 6. Partial view of the mesh (5067 nodes, 9792 triangles)

stream conditions are applied at the inlet and upper boundaries. A homogeneous Neumann condition is used for all the variables at the outlet boundary.

First the influence of the initial and inlet turbulence levels on the results is studied. To this end, two computations are made on the fine mesh, firstly with $10^{-4}u_\infty^2$ as inlet and initial values for k and ε and secondly with $10^{-6}u_\infty^2$. Profiles of the turbulent kinetic energy and the ratio of turbulent eddy viscosity to laminar viscosity across the boundary layer are shown in Figure 7
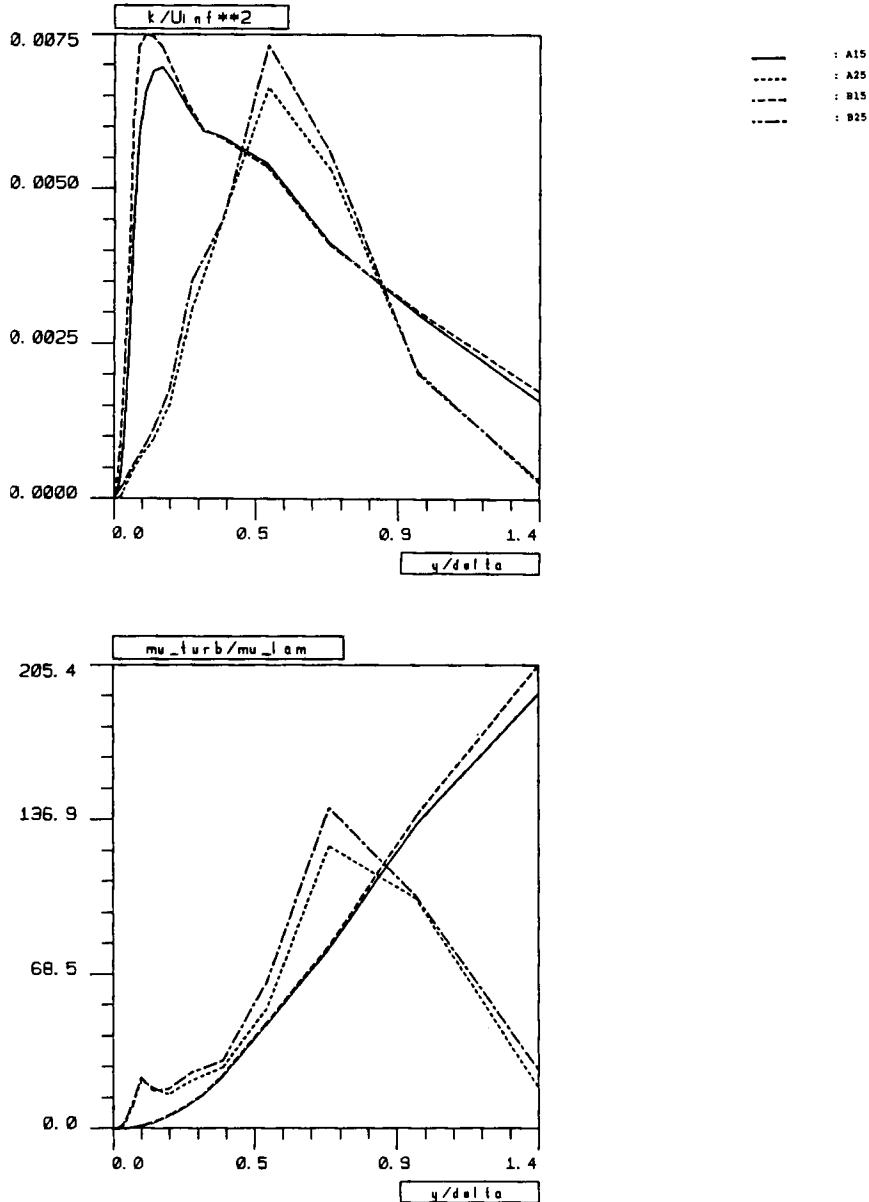
Figure 7. Profiles of k (top) and μ_t/μ_l (bottom) at $x = 0.15$ and 0.25 m from the leading edge: A15 and A25, $k_0 = \varepsilon_0 = 10^{-6}u_\infty^2$; B15 and B25, $k_0 = \varepsilon_0 = 10^{-4}u_\infty^2$

These profiles are given for $x = 0.15$ and 0.25 m (the corner) from the leading edge. We can see that the initial and inlet values levels do not have a great impact on the results in the boundary layer.

In the same way the effect of the local refinement of the mesh on the behaviour of the k–ε model across the shock wave is studied. The computations are made with $10^{-4}u_\infty^2$ as initial and inlet values. Figure 8 shows the behaviour of the kinetic energy across the shock wave located after the corner computed on the coarse and fine meshes. For this we look at the k-values at three locations from the wall (5, 2 and 1 mm). The turbulent intensity grows more significantly across the shock for the fine mesh but we can see that in both cases k quickly takes the same level after the shock. This is somewhat natural, because after the shock we are in a grid turbulence situation (even in the boundary layer), since the production of turbulence is clearly insufficient and the turbulence
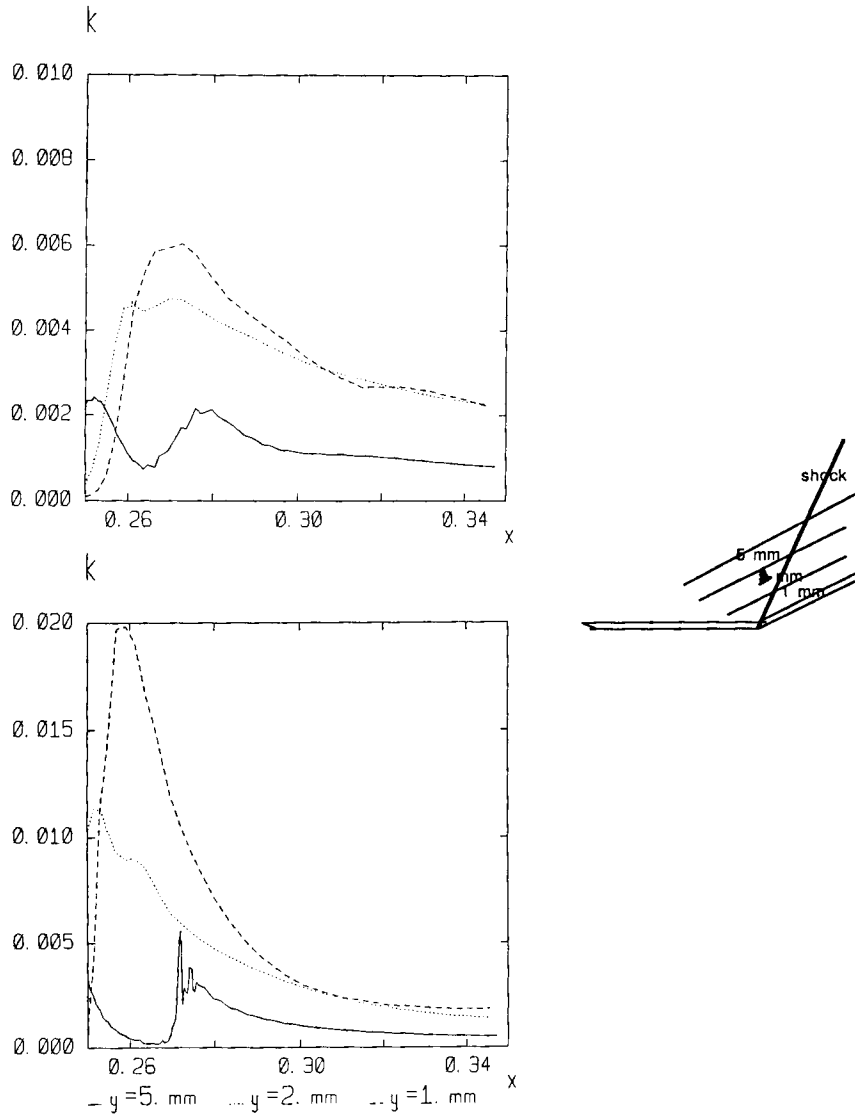
Figure 8. Behaviour of k across the shock wave computed on the coarse (top) and fine (bottom) meshes
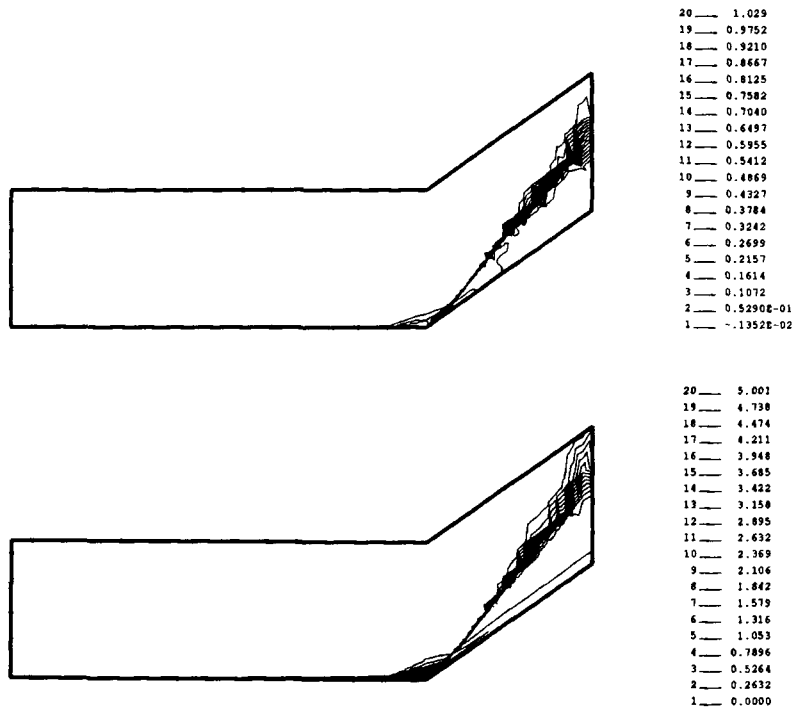
Figure 9. Contour plots of C_p (top) and Mach number (bottom) computed on the fine mesh
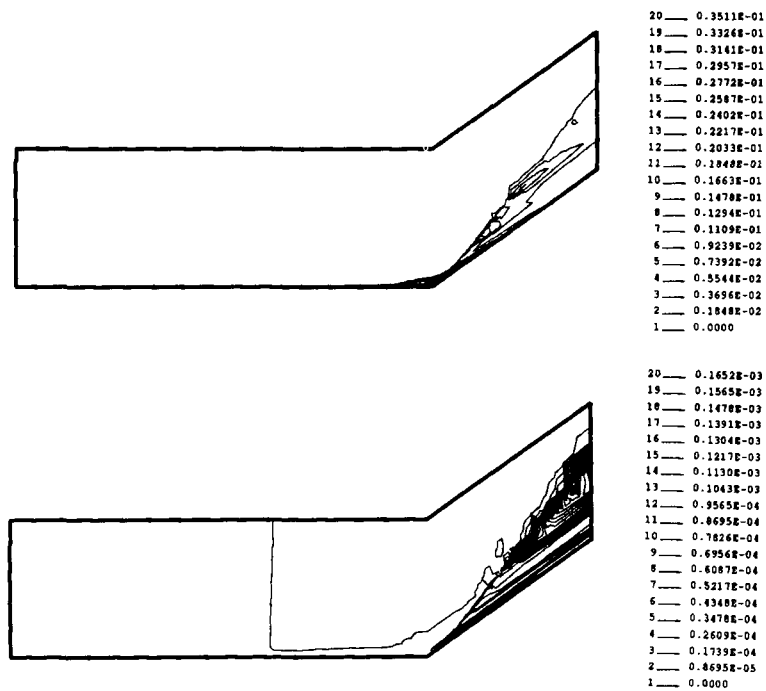
Figure 10. Contour plots of k (top) and μ_t (bottom) computed on the fine mesh

level decreases exponentially. If we continue to refine the mesh, the k-level becomes very large, which has no physical meaning. Thus it seems that our version of the k–ε model is not able to compute correctly the behaviour of the turbulent variables across the shock wave, but this fact does not affect the general flow prediction if the shock is correctly located on a locally refined mesh. This is quite reasonable because of the presence of $\| \nabla u \|$ in the source terms.

Figure 9 shows contour plots of C_p and the Mach number obtained on the refined mesh. The turbulent kinetic energy and eddy viscosity contours are given in Figure 10. The shock is well captured near the corner because the mesh is quite fine, but away from the corner it spreads. This fact has a great impact on the eddy viscosity distribution. Indeed, across the shock region near the
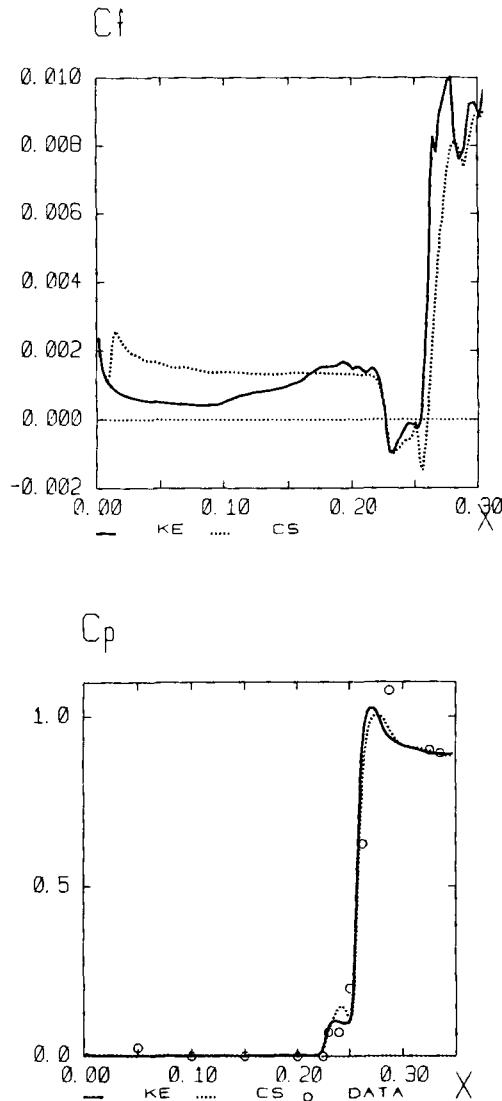
Figure 11. C_f (top) and C_p (bottom) at the wall computed by the k–ε and Cebeci–Smith models (O, data from Reference 13)

corner the eddy viscosity variations stay localized, but away from the corner they perturb the flow more significantly. The eddy viscosity level is 200 times the laminar one on the flat plate and grows across the shock to about $2000\mu_1$. The following results are compared with results obtained using the Cebeci–Smith turbulence model (see Appendix) and with data from Reference 13.

In Figure 11 we show the friction and pressure coefficients at the wall. Better agreement with the experimental pressure coefficient is obtained with our approach. Figure 12 shows the heat flux coefficient at the wall and the velocity profiles through the boundary layer at $x = 0.15$ and 0.25 m computed by the two models.
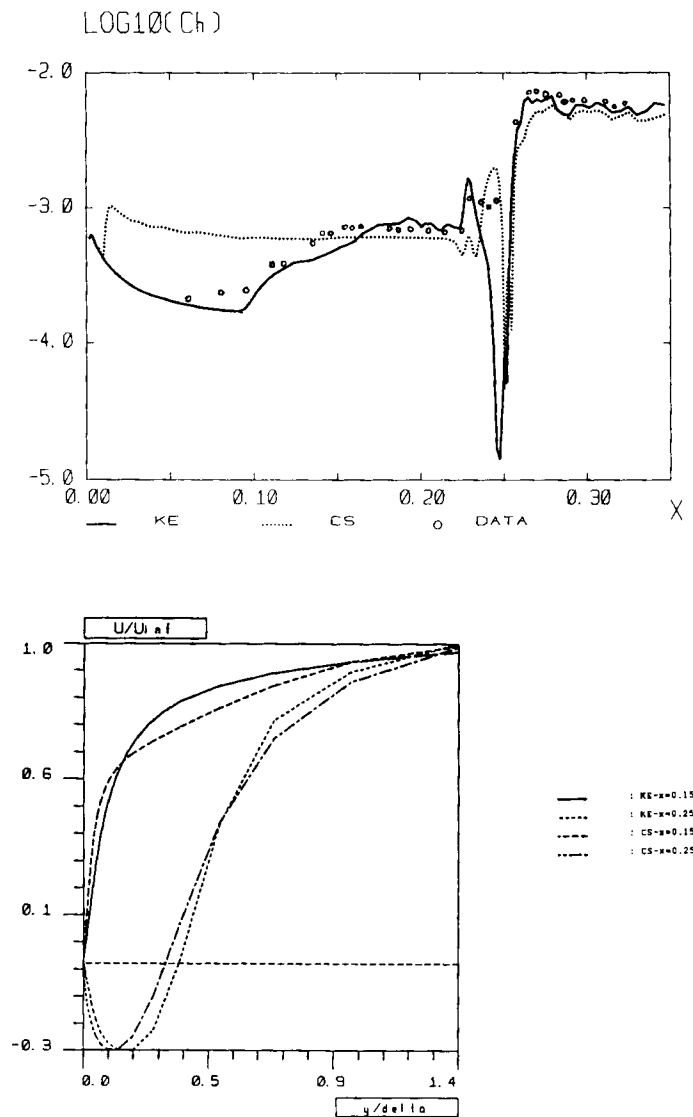
Figure 12. $Log_{10}(C_h)$ at the wall (top) and velocity profile (bottom) through the boundary layer at $x = 0.15$ and 0.25 m from the leading edge computed with the k–ε and Cebeci–Smith models

The wall coefficients are given by

$$C_f = \frac{\tau_w}{\frac{1}{2}\rho_\infty u_\infty^2}, \qquad C_p = \frac{p - p_\infty}{\frac{1}{2}\rho_\infty u_\infty^2}, \qquad C_h = -\frac{\kappa \nabla T}{\frac{1}{2}\rho_\infty u_\infty^3}.$$

We can see that the Cebeci–Smith model predicts a greater recirculation. For the pressure coefficient the agreement with the data is better for the k–ε computation, while for the heat flux coefficient the two-equation model gives a larger flux at the separation and reattachment points. Despite the inability of the model to predict the behaviour of the turbulent quantities across the shock, the k–ε model is interesting for high-speed flows because it predicts quite correctly the most important quantities such as wall coefficients. The prediction of the model in shock wave regions can be improved by introducing the compressibility effects which we have ignored[16,17] in the turbulent flow equations. In the same way, the pressure coefficient is underpredicted by both the k–ε and Cebeci–Smith computations. For the two-equation computation this may be due to the fact that we have neglected the turbulent contribution to the pressure. More precisely, we have ignored $\frac{2}{3}\rho k$ in the pressure expression. This enables us to conserve the same constitutive law
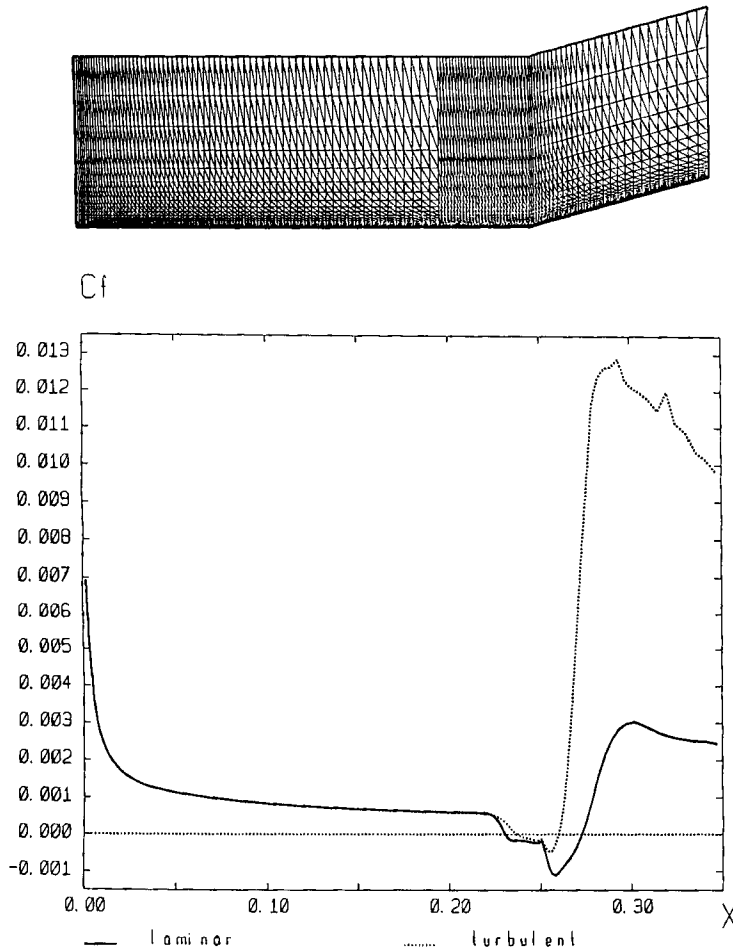
Figure 13. Mesh (top) for the hypersonic compression ramp (4587 nodes, 8832 triangles) and C_f (bottom) at the wall for the laminar and turbulent computations

as in the laminar case.[3] The first computation before refinement took about 90 min on a CRAY-2. After refinement it took 15 min to reach a steady solution.

5.3. Hypersonic compression corner

We study a 15° hypersonic compression corner (test case 3·5 of the Workshop on Hypersonic Flows for Reentry Problems, Antibes, January 1990). The geometry is the same as for the previous case except that the angle at the corner is different. The Mach number is 10 and the Reynolds number 9×10^6 m^{-1}. The free stream temperature is $T_\infty = 50$ K and the wall temperature $T_w = 288$ K. Experiments are available at ONERA.[13]

The mesh is shown in Figure 13. It has 4587 nodes and 8832 triangles. The first spacing normal to the wall is fixed at $1·5 \times 10^{-5}$ m. On this mesh we have done two computations: a completely
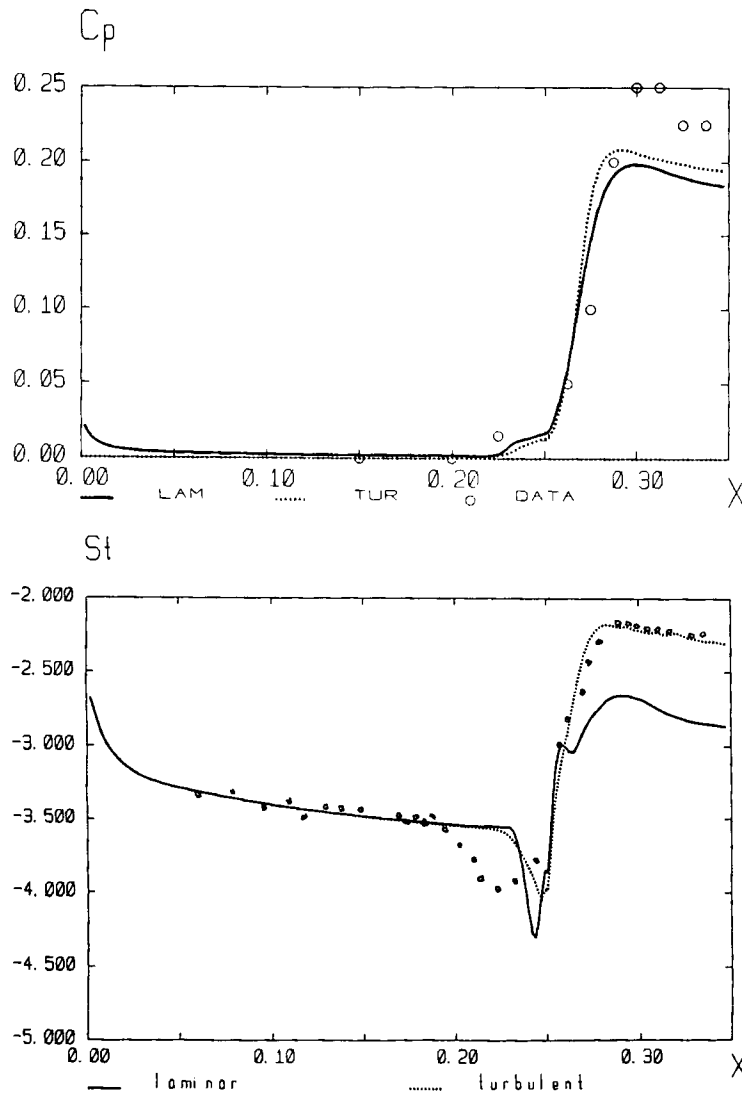
Figure 14. C_p (top) and $S_t = \log_{10}(C_h)$ (bottom) for the hypersonic compression corner for the laminar and turbulent computations ($\bigcirc$, data from Reference 13)

laminar computation (i.e. without any turbulence modelling) and another computation using our k–ε solver. In the second case the turbulence model is started at the corner ($x = 0.25$ m). The initial and boundary conditions are the same as for the previous case. The turbulent computation is done with $k_{in} = \varepsilon_{in} = 10^{-4} u_\infty^2$.

Figure 13 gives a plot of the friction at the wall (laminar and turbulent computations). In the turbulent case we have a smaller recirculation and the level of friction after the corner is higher than for the laminar computation. Plots of the pressure and heat flux coefficients are given in Figure 14. These results are compared with data from Reference 13. Better agreement is obtained with the turbulent computation (especially for the heat flux coefficient after the corner).

On the other hand, the extent of the recirculation bubble is underpredicted by both the laminar and turbulent computations. It seems that in the separation region the mesh is not enough fine. Thus, to observe the dependence of the results upon the mesh refinement, we have done the same computations on a new mesh with 8358 nodes and 16 236 triangles. The pressure coefficients at the wall on the fine and coarse meshes obtained for the turbulent and laminar computations are shown in Figure 15. In the same way the corresponding friction and heat flux coefficients are presented in Figures 16 and 17 respectively. We can see that, especially for the laminar computation on the fine mesh, a higher recirculation region is predicted and better agreement with the data is obtained in this region. On the other hand, in the turbulent computations the extents of the recirculation bubbles are quite similar on the fine and coarse meshes. This proves that our solver is quite mesh-independent.
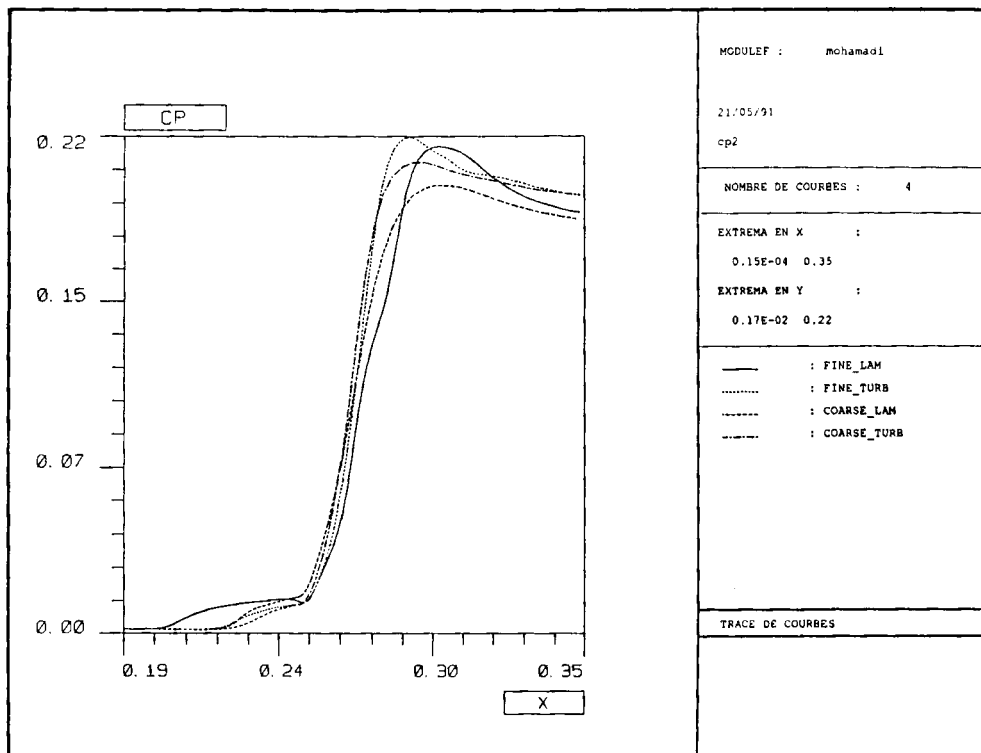
Figure 15. C_p obtained for the laminar and turbulent computations on the fine and coarse meshes

These results are interesting because the nature of the flow is not well known (laminar, transitional or turbulent).[18] The argument concerning the turbulent correction of the pressure remains valid. This may explain why the pressure coefficient is underpredicted although the heat flux coefficient is well predicted on the ramp.

6. CONCLUSIONS

To compute turbulent flows including separation, a two-layer approach and a robust algorithm for k and ε have been proposed.

Several computations have proved the extreme robustness of the k–ε solver. No positivity or boundedness problems have been observed. The two-layer approach clearly appears to be a convenient tool for avoiding near-wall difficulties without requiring supplementary attention. This enables us to compute complex turbulent recirculating flows. Such computations are not possible with a classical wall-law technique, and a modified low-Reynolds-number two-equation model requires considerably more grid points. Moreover, because in the latter model the coefficients of the ε-equation are tuned for the flow over a flat plate, they are not valid in general.

The flow over the cylinder and the hypersonic compression ramp computations show that the results do not depend greatly on the mesh refinement in the direction normal or parallel to the wall.
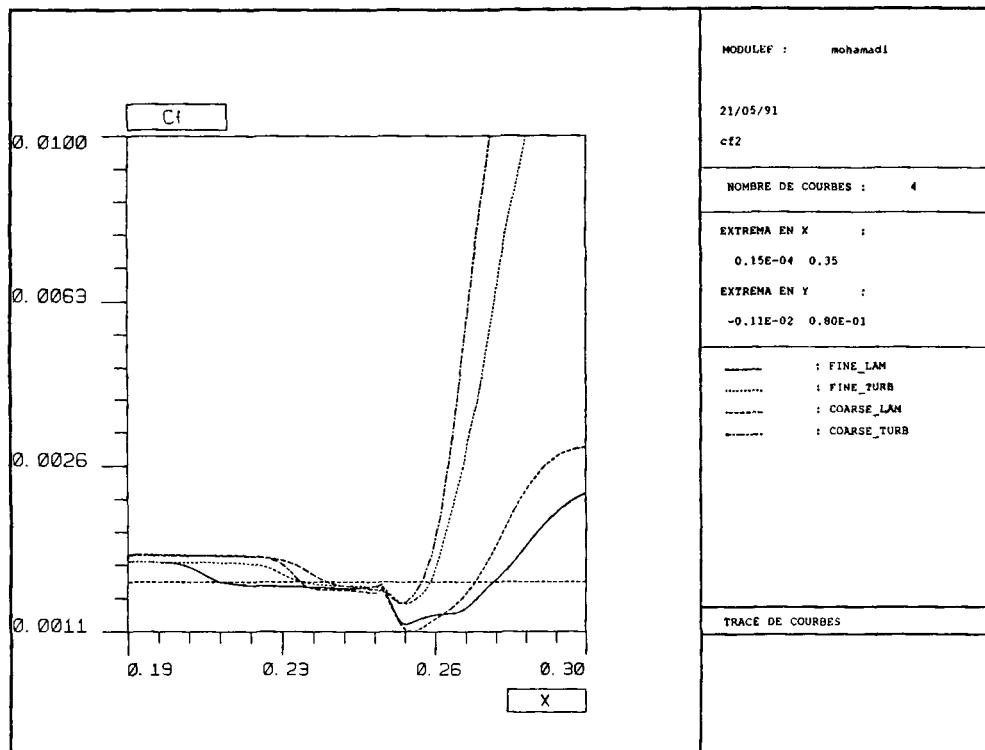
Figure 16. C_f for the laminar and turbulent computations on the fine and coarse meshes
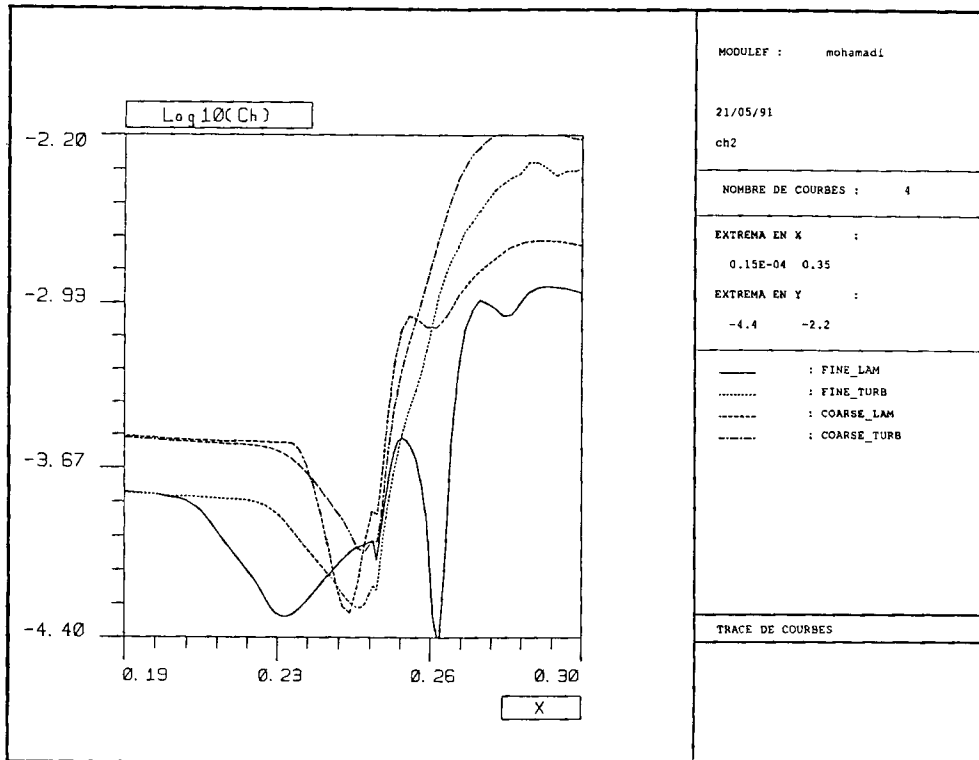
Figure 17. $\text{Log}_{10}(C_h)$ for the laminar and turbulent computations on the fine and coarse meshes

Finally, it is easy to generalize our algorithm and the two-layer approach to 3D configurations. At this moment the solver is able to treat 2D and axisymmetric configurations and the 3D version is under development.

APPENDIX: COMPUTATION WITH ALGEBRAIC EDDY VISCOSITY MODEL

The performances of the two-layer model are compared with an algebraic Cebeci–Smith model where we introduce a Goldberg correction to take into account the separation.[7,19,20] In other words, for separated profiles we take the eddy viscosity from the Cebeci–Smith model, where we use the distance to the backflow bubble edge $(y - y_b)$ instead of the distance to the wall, and in the separation bubble $(y \leqslant y_b)$ we use Goldberg's model. Thus μ_t is given for $y \leqslant y_b$ by

$$\mu_t = 0{\cdot}353\rho u_s y_b \sqrt{\left(\frac{\rho_w}{\rho}\right)\left(A\frac{y}{y_b} + B\right)\left(\frac{1 - \exp[-0{\cdot}5(y/y_b)^2]}{1 - \exp(-0{\cdot}5)}\right)},$$

for $y_b \leqslant y \leqslant y_c$ by

$$\mu_t = \rho l^2 |\omega|$$

and for $y_c \leqslant y$ by

$$\mu_t = \alpha u_e \delta_i \left[1 + 5 \cdot 5 \left(c_{kl} \frac{y - y_b}{y_{av}} \right)^6 \right]^{-1},$$

where

$$c_\mu^* = 0 \cdot 7, \qquad A = -\left(\frac{c_\mu^*}{2} \right)^{9/5}, \qquad B = \left(\frac{c_\mu^*}{2} \right)^{3/5} - A,$$

$$u_s = \sqrt{\left[v_{tm} \left(\frac{\partial u_t}{\partial y} \right)_{max} \right]}, \qquad l = \kappa(y - y_b) \left[1 - \exp\left(-\frac{y - y_b}{A} \right) \right],$$

$$u_e \delta_i = \int_{y_b}^{y*} y |\omega| \, dy, \qquad y_{av} = \frac{\int_{y_b}^{y*} y^2 |\omega| \, dy}{\int_{y_b}^{y*} y |\omega| \, dy},$$

with $\alpha = 0 \cdot 0168$, $c_{kl} = 0 \cdot 45$, ω the vorticity and v_{tm} the value of $v_t = \mu_t / \rho$ at the location of $(\partial u_t / \partial y)_{max}$. On the other hand, y^* is taken such that $F(y^*) \leqslant 0 \cdot 5 F_{max}$, with $F = y |\omega| [1 - \exp(-y/A)]$. Of course, for attached flows we have only two levels in the previous scheme ($y_b = 0$).

REFERENCES

1. V. C. Patel, W. Rodi and G. Scheuerer, 'Turbulence models for near-wall and low Reynolds number flows: a review', *AIAA J.*, **23**(9), 1308–1319 (1984).
2. V. C. Patel and H. C. Chen, 'Near-wall turbulence models for complex flows including separation', *AIAA J.*, **26**(6), 641–648 (1988).
3. B. Mohammadi, 'A stable algorithm for the k–ε model for compressible flows', *INRIA Rep. 1355*, 1990.
4. A. G. Hutton, R. M. Smith and S. Hickmott, 'The computation of turbulent flows of industrial complexity by a finite element method—progress and perspective', *Int. j. numer. methods fluids*, **7**, 1277–1298 (1987).
5. R. M. Smith, 'On the finite element calculation of turbulent flow using the k–ε model', *Int. j. numer. methods fluids*, **4**, 303–319 (1984).
6. B. Cardot, B. Mohammadi and O. Pironneau, 'A few tools for the implementation of turbulence models in Navier–Stokes solvers', in M. D. Gunzburger and R. A. Nicolaides (eds), *Incompressible CFD—Trends and Advances*, Cambridge University Press, Cambridge, 1991.
7. P. Rostand, 'Sur une méthode de volumes finis en maillage non structuré pour le calcul d'écoulements visqueux compressibles', *Ph.D. Thesis*, Université Paris VI, 1989.
8. F. Angrand, and A. Dervieux, 'Some explicit triangular finite element schemes for the Euler equations', *Int. j. numer. methods fluids*, **4**, 749–764 (1984).
9. F. Angrand, 'Viscous perturbations for the compressible Euler equations, application to the numerical simulation of compressible viscous flows', *Proc. GAMM Workshop on Numerical Simulation of Compressible Navier–Stokes Flows*, Nice, December 1985, Vieweg, 1982.
10. S. Majumdar and W. Rodi, 'Numerical calculations of turbulent flow past circular cylinders', *Proc. 3rd Symp. on Numerical and Physical Aspects of Aerodynamic Flows*, Long Beach, CA, January 1985.
11. E. Achenbach, 'Distribution of local pressure and skin friction around a circular cylinder in cross-flow up to $Re = 5.10^6$', *J. Fluid Mech.*, **34**, 625–639 (1968).
12. *GAMM Workshop on Numerical Simulation of Computational Euler Flows*, Notes on Numerical Fluid Dynamics, Vieweg, 1987.
13. J. Delery and M. C. Coet, 'Experiments on shock-wave/boundary-layer interactions produced by two-dimensional ramps and three-dimensional obstacles', *Proc. Workshop on Hypersonic Flows for Reentry Problems*, Antibes, January 1990, Springer-Verlag.
14. C. Pouletty, 'Génération et optimisation de maillages en éléments finis, applications à la résolution des équations de la mécanique des fluides', *Thèse de Docteur Ingénieur*, Ecole Centrale, Paris, 1985.
15. B. Palmerio, 'Self adaptive FEM algorithms for the Euler equations', *INRIA Rep. 338*, 1985.

16. F. Grasso and C. Speziale, 'Supersonic flow computations by two-equation turbulence modelling', *AIAA Paper 89-1951*, 1989.
17. D. Vandromme, 'Contribution à la modélisation et la prédiction d'écoulements turbulents à masse volumique variable', *Thesis*, University of Lille, 1983.
18. J. L. Stollery, 'Some viscous interactions affecting the design of hypersonic intakes and nozzles', *Lect. Workshop on Hypersonic Flows for Reentry Problems, Part II*, Antibes, 1991, to appear.
19. T. Cebeci and A. Smith, *Analysis of Turbulent Boundary Layers*, Academic, New York, 1974.
20. U. C. Goldberg, 'Separated flow treatment with a new turbulence model', *AIAA J.*, **24**, 1711–1713 (1986).